RESEARCH

Open Access

Human–exoskeleton interaction portrait

Mohammad Shushtari[1], Julia Foellmer[2] and Arash Arami[1,3*]

Abstract

Human–robot physical interaction contains crucial information for optimizing user experience, enhancing robot performance, and objectively assessing user adaptation. This study introduces a new method to evaluate human–robot interaction and co-adaptation in lower limb exoskeletons by analyzing muscle activity and interaction torque as a two-dimensional random variable. We introduce the interaction portrait (IP), which visualizes this variable's distribution in polar coordinates. We applied IP to compare a recently developed hybrid torque controller (HTC) based on kinematic state feedback and a novel adaptive model-based torque controller (AMTC) with online learning, proposed herein, against a time-based controller (TBC) during treadmill walking at varying speeds. Compared to TBC, both HTC and AMTC significantly lower users' normalized oxygen uptake, suggesting enhanced user-exoskeleton coordination. IP analysis reveals that this improvement stems from two distinct co-adaptation strategies, unidentifiable by traditional muscle activity or interaction torque analyses alone. HTC encourages users to yield control to the exoskeleton, decreasing overall muscular effort but increasing interaction torque, as the exoskeleton compensates for user dynamics. Conversely, AMTC promotes user engagement through increased muscular effort and reduces interaction torques, aligning it more closely with rehabilitation and gait training applications. IP phase evolution provides insight into each user's interaction strategy formation, showcasing IP analysis's potential in comparing and designing novel controllers to optimize human–robot interaction in wearable robots.

Keywords Exoskeleton, Physical Interaction, Control

Introduction

Assistive and rehabilitation robotics are gaining increasing attention as they deliver a more substantial dose of exercise to users, enhancing their functionality and quality of life while reducing the workload of physical therapists [1, 2]. Despite recent advancements, including human-in-the-loop optimization to improve exoskeleton assistance [3–6], these robotic systems still lack the sophistication to automatically fine-tune the level of support required for each individual user effectively [7,

8]. This personalized touch, instinctive for physical therapists in traditional therapy sessions, remains a challenge for robots due to the lack of a unified metric for monitoring and quantifying human–exoskeleton interaction.

A range of studies have used quantitative metrics that describe aspects of human–exoskeleton interaction or its consequences. For instance, Postol et al. examined the metabolic cost of exercising with a robotic exoskeleton, noting that both healthy and neurologically impaired participants increased their VO2 levels during exoskeleton-assisted exercise, with stroke participants showing a greater reduction after 12 weeks of therapy [9]. Witte et al. explored the energy economy of human running with powered and unpowered ankle exoskeleton assistance, finding that optimized powered assistance significantly improved energy economy compared to running in normal shoes [10]. While low metabolic cost and improved energy economy could be indicators of effective assistance and reduction of human–robot physical

*Correspondence:
Arash Arami
arash.arami@uwaterloo.ca
[1] Department of Mechanical and Mechatronics Engineering, University of Waterloo, Waterloo, ON N2L 3G1, Canada
[2] Mechanics and Ocean Engineering Department, Hamburg University of Technology, 21071 Hamburg, Germany
[3] Toronto Rehabilitation Institute (KITE), University Health Network, Toronto, ON M5G 2A2, Canada

Shushtari *et al. Journal of NeuroEngineering and Rehabilitation*   (2024) 21:152

Page 2 of 20

conflicts, these metrics do not directly assess the interaction quality, e.g., whether the user was actively engaged in movement or not. Zhu et al. compared the lower-limb muscle synergies between users wearing and not wearing exoskeletons and during exoskeleton-assisted gait training in post-stroke patients. They found that wearing the exoskeleton altered synergy patterns towards those of able-bodied participants [11]. While similar muscle synergy patterns could indicate an increased chance of motor recovery, uncertainties remain due to the sensitivity of the obtained synergies to the choice of optimization setting. Muscle synergies do not provide details of human–robot interaction in terms of who is leading the control of motion, or following, and whether they are actively participating, resisting or remaining passive. Ingraham et al. focused on user preference in exoskeleton control by having participants self-tune the magnitude and timing of peak torque using a touch screen tablet, demonstrating that individuals can reliably identify their preferred assistance settings, which varied with walking speed and device exposure [12]. Küçüktabak et al. looked at interaction power to assess human–exoskeleton interaction. The study included an analysis of the power flow between the exoskeleton and the user, particularly focusing on the interaction torques and power and their effects on muscle activity [13]. Dalley et al. developed a controller that enabled continuous joint motion, which in turn increased walking speed and speed control [14]. Durandau et al. also demonstrated that using a neuromechanical model-based control approach enabled significant reductions in both biological joint torques and electromyograms (EMGs) across various walking conditions and transitions [5]. The metrics used in these studies were not chosen to directly quantify human–exoskeleton interaction; instead, they served as criteria for tuning exoskeleton control. For instance, reducing metabolic cost or muscular effort has been considered a desirable outcome, regardless of the underlying mechanisms. However, a reduction in metabolic cost could result from user disengagement, which is undesirable in rehabilitation. Therefore, a multifaceted approach that combines various metrics is needed to accurately indicate the user's response to different exoskeleton control strategies.

Questionnaires have been used in various studies [15–18] and despite being subjective showed to be valuable in revealing aspects of user's perception about their interaction with the exoskeleton. Pisotta et al. developed a four-factor questionnaire to assess user experience with lower limb exoskeletons [15], while Muijzer-Witteveen et al. utilized a questionnaire to identify missing sensory information and preferences for feedback methods among individuals with Spinal Cord Injury using exoskeletons [16]. Additionally, Lee et al. emphasized the importance of establishing a methodology for user evaluation of exoskeletons to enhance safety, convenience, and usability. They highlighted the need for detailed evaluation elements and considerations for different user classes [17].

Although separate performance indicators are utilized in the field, none fully encapsulate the nuances of human–robot physical interaction, obstructing the precise adjustment and customization of lower limb exoskeleton support [19]. Questionnaires are also subjective and prone to biases.

Quantifying and controlling human–exoskeleton interaction plays a key role in optimizing the user experience and performance of lower limb exoskeletons for rehabilitation as well as power augmentation applications [20]. In power augmentation scenarios, the user retains full autonomy, and the exoskeleton follows user commands directly or indirectly by interpreting their intended motion. In case of disagreement between the user and the exoskeleton, the exoskeleton must relinquish control in favor of the user [21, 22]. However, in the context of rehabilitation exoskeletons, human–exoskeleton interaction control is more challenging due to two primary factors. First, the user-performed motion is not always reliable due to musculoskeletal or motor impairments [23] undermining the quality of decoded intention solely based on user-robot physical interaction. Second, the exoskeleton should encourage the user to maximize their engagement in motion when possible and assist or correct when the user is unable to perform the motion correctly [24, 25]. Consequently, the exoskeleton must seamlessly transition between the leader and follower roles [26].

To determine the appropriate control strategy for human augmentation and rehabilitation applications, it is crucial to understand human–exoskeleton adaptation as an indicator of how individuals respond to specific exoskeleton control strategies concerning shared motion control [27]. Adaptation in our context refers to the observed changes in user interaction strategy rather than adaptation of neuromotor activities to a specific pattern or to achieve a goal. These changes in behaviors indicate how users adapt their interaction strategy to the exoskeleton's control over time. However, it is worth noting that the emerged interaction strategy can be formulated as a motor learning in a dyadic task.

In power augmentation, the ideal scenario involves users to contribute primarily by guiding the motion, without physical exertion [5]. The exoskeleton takes the responsibility of moving the human body by applying interaction torques or forces demonstrated by reduced muscle activity or metabolic rates [4]. Conversely, in rehabilitation, users must often be guided to increase their muscle activity and actively engage in motion

control [28]. The human–exoskeleton interaction torques exhibit a dual behaviour in this context. When the user performs the motion correctly, the exoskeleton must transparently follow the user, resulting in zero interaction torques [13]. However, when motion correction is required, the exoskeleton controller should intervene. This intervention creates a conflict that necessitates an increase in the interaction torque to rectify the motion. Neither muscular effort nor interaction torques alone can discern the aforementioned conditions. For example, an increase in muscular effort may stem from human–exoskeleton disagreement [23], while it can also signify that the human user is engaged in walking and relies on their motor capacity rather than on exoskeleton assistance. Therefore, to compare different controllers in such cases, interaction torque needs to be considered alongside muscular effort. A low level of interaction torque coupled with higher muscular effort suggests no physical disagreement, indicating that the exoskeleton is following the user and the user is walking with minimal assistance. Conversely, a higher level of interaction torque along with high muscular effort indicates that the user and exoskeleton do not share the same desired motion patterns, and they are fighting for control [26]. Therefore, determining the suitability of a controller for either power augmentation or rehabilitation applications requires a co-analysis of muscular effort and interaction torque.

Inspired by the above reasoning, we propose evaluating human–exoskeleton physical interaction by co-analyzing the variation of muscular effort ($\Delta\mu$) and interaction torques ($\Delta\tau$) as a 2D random variable in the $\Delta\tau - \Delta\mu$ space, which draws the interaction portrait (IP), i.e., the distribution of the $\Delta\tau - \Delta\mu$ random variable. IP stochasticity is induced by natural variation in human motor control and motor unit recruitment. According to Fig. 1, we show that the phase of the IP distribution (in polar coordinates) indicates whether the human–exoskeleton interaction is developing toward yielding motion control to the human, to the exoskeleton, or toward an increase in human–exoskeleton physical disagreement. Moreover, the temporal analysis of the IP phase reveals how this interaction evolves over time.
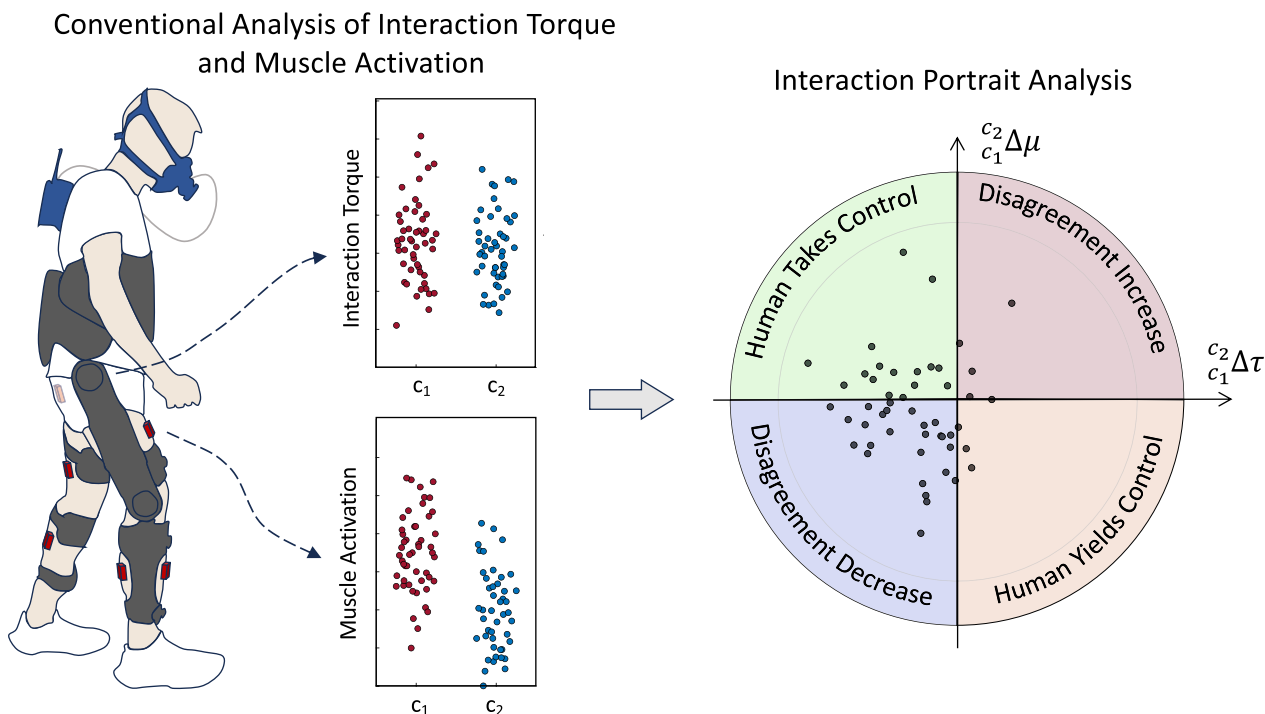
Fig. 1 Regions of interaction portrait (IP). Each quadrant of the circle corresponds to different human–exoskeleton interaction modes determined by the variation of the normalized total muscle activation ($^{c_2}_{c_1}\Delta\mu$) with respect to the normalized total interaction torque ($^{c_2}_{c_1}\Delta\tau$) between controllers c_1 and c_2, respectively. The first quadrant (red) indicates increased disagreement between the user and exoskeleton, resulting in an increase in both muscle effort and the total interaction torque. The second quadrant (green) determines the co-adaptation of the user toward participating in the motion as much as possible and leading the motion. The third quadrant (blue) denotes the decrease in total interaction torque and the total muscle effort, associated with the decrease in human–exoskeleton disagreement. Finally, the fourth quadrant (orange) denotes the condition at which the user yields control of the motion to the exoskeleton and minimally activates their muscles. In this case, muscle activation decreases while the total interaction increases since the exoskeleton has to carry the user's body (passive dynamics) in addition to the exoskeleton dynamics

This metric is utilized to compare a time-based torque controller (TBC), a recently developed hybrid torque controller (HTC), that computes the required joint torque based on kinematic states [29], and a novel torque controller proposed in this paper called adaptive model-based torque controller (AMTC), that learns the user's desired trajectory and employs the exoskeleton's dynamical model to generate feedforward torques. We hypothesize that users will adopt different interaction strategies with these three controllers, expecting difficulty in maintaining a consistent strategy with TBC, as it is blind to the user's gait variability. Thus, we expect both HTC and AMTC to result in lower human–exoskeleton physical disagreement compared to TBC. Also, because of the intuitive adaptation mechanisms in the AMTC, we anticipate users to adapt to a consistent strategy faster with AMTC compared to HTC. The proposed interaction portrait analysis enables quantitative study of the adaptation mechanism in the case of each of these controllers. It is worth noting that TBC, HTC and AMTC were chosen to showcase the IP analysis as the controller adaptation methods vary among these controllers: from none, to implicit (state-based torque computation), to explicit (reference trajectory adaptation), respectively.

Methods

Feedforward control strategies

This section describes three controllers tested in our study.

Time-based torque controller

Figure 2A depicts the block diagram of the Time-Based Torque Controller (TBC). This controller utilizes lookup tables to determine the desired joint torques $\boldsymbol{u}_E$ by considering both the gait phase ($\phi(t)$) and the estimated gait speed (v). To construct the lookup table, measurements of exoskeleton joint torques were taken at different speeds while a participant walked with the exoskeleton governed by a high-gain PD controller. The participant was asked to exert the minimum voluntary effort during walking. The joint trajectories were controlled based on reference trajectories derived from the participant's walking without the exoskeleton. The input gait phase to the lookup table was obtained by dividing the stride length,
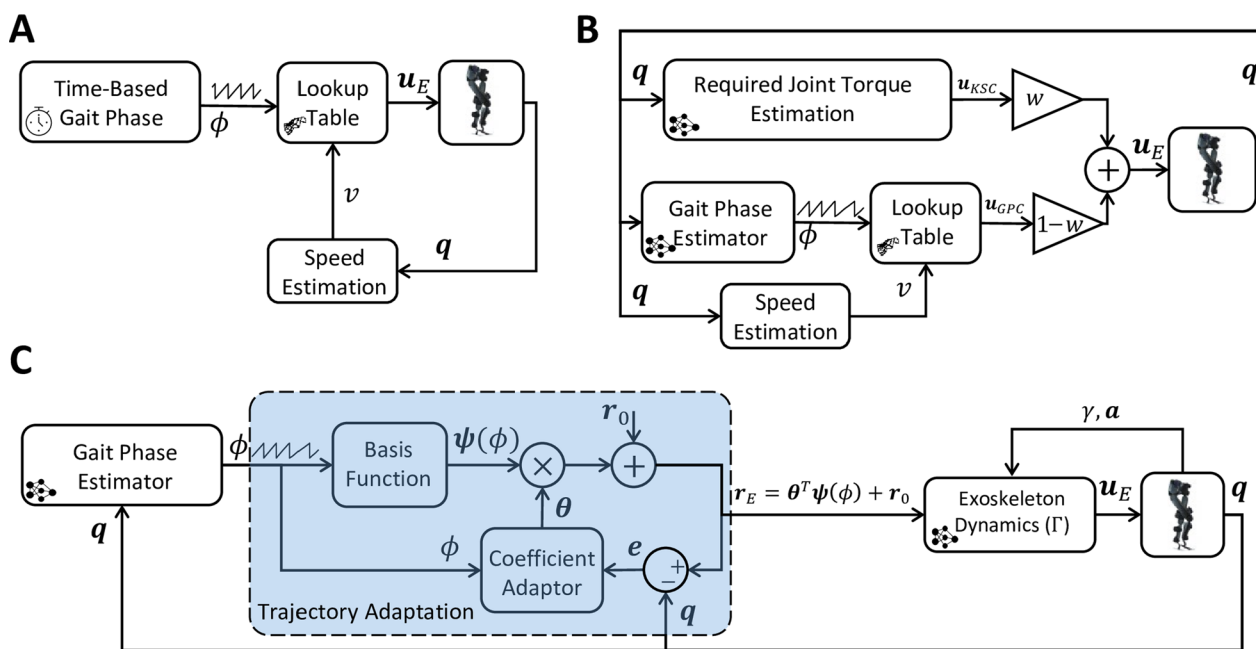
Fig. 2 Block diagram of TBC, HTC, and AMTC controllers. **A** Block diagram of the Time-Based Controller (TBC). A time-based gait phase along with the estimated gait speed are fed into a lookup table to determine the applied torque to the exoskeleton joints according to joint torque data recorded from the exoskeleton during high-gain joint control with the user passively following the exoskeleton (with the minimum voluntary contribution to the gait). **B** Hybrid Torque Controller (HTC) consisted of a data-driven estimator of the required joint torque along with a lookup table-based torque controller similar to the TBC. In this case, however, the gait phase is determined according to the exoskeleton states rather than time. The torque from the two different pipelines is finally combined with the weight of $w = 0.75$ and $1 - w = 0.25$ to form the applied torque to the exoskeleton. **C** Block diagram of the Model-Based Torque Controller (AMTC). The gait phase is estimated according to the exoskeleton joint angles and then fed into a trajectory adaptation block which learns the joint trajectory of the participant in real time and uses that trajectory as the reference for the exoskeleton to be fed into the forward dynamics of the exoskeleton to determine the feedforward joint torques

calculated using the exoskeleton joint angles (q), by the stride time updated at each heel strike. For this controller, the gait phase ($\phi(t)$) was generated based on the desired gait speed, following the formula $\phi(t) = mod(t, T)$, where T represents the average measured stride time when the participant walked without the exoskeleton at the desired gait speed. For more detailed information about the construction of the lookup table and the gait speed estimator, refer to [29].

Hybrid Torque Controller

Figure 2B presents the block diagram of the Hybrid Torque Controller (HTC), which combines the torque outputs of two distinct controllers [29]: the Kinematic State Dependent Controller (KSC) and the Gait Phase Dependent Controller (GPC). The KSC incorporates an inverse dynamics model and an Artificial Neural Network (ANN) that compute the required biological torque for the user based on the kinematic measurements [30]. On the other hand, the GPC adopts the same structure as the TBC mentioned earlier, however, instead of relying on a time-based gait phase, it utilizes a real-time estimation of the gait phase derived from the kinematic measurements [31]. The outputs of these two controllers are linearly combined in the HTC: $u_E = w u_{KSC} + (1 - w) u_{GPC}$, where the blending weight for all users is $w = 0.75$, representing the weight assigned to the KSC output.

Adaptive model-based Torque control

The Adaptive Model-based Torque Control (AMTC) depicted in Fig. 2C, leverages the estimated dynamics of the exoskeleton to generate joint torques for control. According to [32], the interaction between the Indego exoskeleton and the human in the sagittal plane can be described by the following dynamical model:

$$\boldsymbol{\Gamma}(\gamma, \dot{\gamma}, \ddot{\gamma}, \boldsymbol{a}, \boldsymbol{q}, \dot{\boldsymbol{q}}, \ddot{\boldsymbol{q}}) = \boldsymbol{u}_E + \boldsymbol{u}_{int}, \tag{1}$$

where $\gamma \in \mathbb{R}$ and $\boldsymbol{a} \in \mathbb{R}^2$ denote the exoskeleton thigh angle with respect to the gravity vector and its acceleration in the sagittal plane, respectively, $\boldsymbol{q} = [q_{h,r}; q_{k,r}; q_{h,l}; q_{h,l}] \in \mathbb{R}^4$ represents the exoskeleton hip and knee joint angles, $\boldsymbol{u}_E \in \mathbb{R}^4$ denotes the exoskeleton applied motor torques, and $\boldsymbol{u}_{int} \in \mathbb{R}^4$ represents the torques arising from the human–exoskeleton interaction. The AMTC controller employs a dynamic compensatory approach. In a dynamic compensator, the exoskeleton's applied torques are set equal to the exoskeleton's passive dynamics ($\boldsymbol{u}_E = \boldsymbol{\Gamma}(\gamma, \dot{\gamma}, \ddot{\gamma}, \boldsymbol{a}, \boldsymbol{q}, \dot{\boldsymbol{q}}, \ddot{\boldsymbol{q}})$) which ideally results in the transparency of the exoskeleton ($\boldsymbol{u}_{int} = 0$). However, in AMTC, the exoskeleton torques are computed using the desired joint angles instead of the current (actual) joint angles:

$$\boldsymbol{u}_E = \boldsymbol{\Gamma}(\gamma, \dot{\gamma}, \ddot{\gamma}, \boldsymbol{a}, \boldsymbol{r}_E, \dot{\boldsymbol{r}}_E, \ddot{\boldsymbol{r}}_E), \tag{2}$$

where $\boldsymbol{r}_E \in \mathbb{R}^4$ are the desired exoskeleton joint angles. This approach ensures the exoskeleton remains transparent only when the user's joint motions match the desired trajectories. Otherwise, the exoskeleton will assist or resist the user's motion depending on the consistency between the user's intended motion and the exoskeleton's desired trajectories. To ensure that the exoskeleton always assists the user and avoids resisting their motion, the reference trajectory of the exoskeleton needs to be synchronized temporally with the user's desired motion and matched spatially to their intended gait pattern. Temporal synchronization is achieved by defining the exoskeleton's reference trajectory as a function of the estimated gait phase computed from the exoskeleton's joint angles ($\boldsymbol{r}_E(t) = \boldsymbol{r}_E(\phi(\boldsymbol{q}))$). Spatial consistency is ensured by adapting the reference trajectory based on the minimization of the error between the exoskeleton's reference trajectory and its current joint angles ($\boldsymbol{e} = \boldsymbol{r}_E - \boldsymbol{q}$). At each joint, the reference trajectory is defined as $r_E = r_0(\phi) + \Delta(\phi)$, where r_0 represents the initial reference trajectory of the exoskeleton, and $\Delta(\phi) = \boldsymbol{\theta}^T \boldsymbol{\psi}(\phi)$ is the modification term. Here, $\boldsymbol{\psi}(\cdot)$ represents the Fourier series basis functions with up to m harmonics, and $\boldsymbol{\theta}$ represents the coefficients of the Fourier series that are adapted similar to [23]. The adaptation rule is then derived to minimize $J = 0.5e^2$ using Gradient Descent (with a learning rate of $\epsilon = 0.05$):

$$\dot{\boldsymbol{\theta}} = -\epsilon \frac{\partial J}{\partial \boldsymbol{\theta}} = -\epsilon \frac{\partial J}{\partial e} \frac{\partial e}{\partial r_E} \frac{\partial r_E}{\partial \Delta} \frac{\partial \Delta}{\partial \boldsymbol{\theta}} = -\epsilon e \boldsymbol{\psi}(\boldsymbol{\phi}). \tag{3}$$

Look at Fig. 5C for an example of joint torque generated by each of the described controllers, temporally normalized with respect to the gait phase.

Experimental setup

The experimental setup comprised a split-belt instrumented treadmill (Bertec, USA), providing ground reaction forces (GRF) on each belt, a lower limb exoskeleton (Indego, ekso Bionics, USA) with actuated hip and knee joints, fourteen wireless EMG sensors (Trigno, Delsys, USA), and a COSMED K5 wearable metabolic system (Albano Laziale, Rome, Italy) to measure oxygen uptake (VO2). Additionally, four Inertial Measurement Units (IMUs) (Physilog 6 s, Gait Up SA, CH) are employed to measure gait spatiotemporal parameters. The exoskeleton encoders, IMUs, load cells, and EMG sensors have sampling rates of 200 Hz, 128 Hz, 1000 Hz, and 2000 Hz, respectively. Following appropriate skin treatment, EMG sensors were placed on Gluteus Maximus (GMx), Biceps Femoris (BF), Rectus Femoris (RF), Vastus Medialis

(VM), Gastrocnemius Medialis (GM), Soleus (Sol), and Tibialis Anterior (TA) muscles of each leg. Spatiotemporal gait parameters such as Minimum Toe Clearance (minTC), Maximum Heel Clearance (maxHC), Stance Time Percentage, and Stride Length are computed using the IMUs, as validated in previous studies [33, 34]. Before recording data for each subject, the COSMED K5 underwent a calibration process following a standardized procedure [35]. Figure 3A illustrates the exoskeleton and the placement of the sensors within the experimental setup.

Experimental protocol

The experiment consisted of three blocks, each involving participants walking on the treadmill with the exoskeleton controlled by one of three different controllers: TBC, HTC, or AMTC. The order of the blocks was varied among participants to mitigate any potential order effects. Within each block, participants walked at 0.4, 0.6, and 0.8 m/s, respectively. Each speed lasted for a duration of 100 s. For an illustration of the treadmill speed and the order of the controllers applied to the exoskeleton for participant #9, refer to Fig. 3B. Participants also walked on the treadmill without exoskeleton at the same three speeds to obtain baselines for metabolic rate and muscular effort, ground reaction forces, and gait spatiotemporal parameters.

The maximum walking speed is limited to 0.8 m/s due to the exoskeleton's weight and safety concerns. Lower walking speeds are prioritized in rehabilitation settings, where slow walking is crucial during the early stages of recovery leading to very different walking patterns and interaction with the exoskeleton. Additionally, the cost function of gait varies with speed due to gravity, potentially leading to different adaptation strategies at different speeds [36].

A total of nine able-bodied participants (5 males and 4 females, age: 23.4 ± 4.2 years, mass: 73.6 ± 20.2 kg, height: 176.7 ± 9.6 cm) participated in the study. All participants provided informed written consent prior to the experiments. The study protocol and procedures received ethical approval from the University of Waterloo Clinical Research Ethics Committee (ORE#41794). The study adhered to the principles outlined in the Declaration of Helsinki. The anonymized data is available at https://doi.org/10.6084/m9.figshare.25365772.

Data analysis

Muscle activation

The EMG data was bandpass filtered, with cutoff frequencies of 5 and 500 Hz. The signal was then full-wave rectified and its envelope was computed by applying a moving average with a window of 100 ms. Each EMG signal is normalized by its respective maximum voluntary contraction
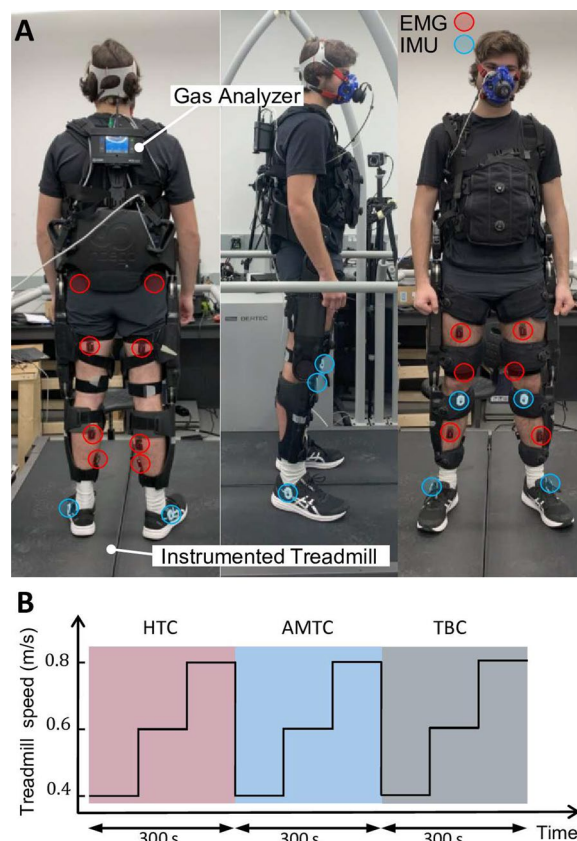
Fig. 3 A Dorsal, lateral, and frontal view of a participant with the Indego exoskeleton with active hip and knee joints. The participant is standing on the Bertec treadmill with two speed-controlled belts equipped with individual loadcells underneath each of them for GRF monitoring. Muscle activation is measured from both right and left leg muscles using EMG sensors. Gait up IMUs are clipped to the outer side of the shoes, right below ankle joints to measure the spatiotemporal parameters of gait. Oxygen uptake of the participant is measured and recorded at each breath through a mask connected to the gas analyzer carried at the back of the participant. **B** Treadmill speed changes while experimenting with the HTC, AMTC, and the TBC controllers. The order of the controllers was specific to participant #9 and varied for other participants. Participants walked with each controller for 300 s divided by three 100-second walking periods during each the treadmill speed was set to 0.4, 0.6, and 0.8 m/s, respectively

(MVC), computed for each muscle as the maximum measured contraction during walking on the treadmill (maximum across with and without the exoskeleton walking). The average muscle effort [37, 38] is computed for each muscle at each stride s as

$$\mu_{m,s} = \frac{1}{T_s} \int_{T_s} e_m^2(t)dt,$$

where $e(t)$ is the filtered EMG signal, T_s is the duration of stride s computed by heel-strike events obtained from

vertical Ground Reaction Force (GRF) measurements, $m \in \{$GMx, BF, RF, VM, GM, Sol, TA$\}$, is the muscle index. The muscle effort over all strides with controller $c \in \{$ TBC, HTC, AMTC$\}$ and speed $v \in \{0.4, 0.6,$ and 0.8 m/s$\}$ is, therefore, computed as

$$\mu_{c,v,m} = \sum_{s \in S_{c,v}} T_s \mu_{m,s},$$

where $S_{c,v}$ is the set of all strides during walking with exoskeleton at treadmill speed v with controller c. Finally, the total muscular effort ($\mu_{c,v}^{tot}$) was determined as the weighted average of the muscle efforts across all muscles. Physiological cross-sectional areas (PCSA) of muscles, obtained from [39], were employed as the weights for total muscular effort computation. This weighting scheme partly accounts for the differences in force contributions across muscles. It is worth noting that the torques generated by particular muscles also depend on their moment arms and the interaction between active and passive (tendon) structures, however, the aim of our EMG analysis is to estimate the overall muscular effort rather than the joint torque or power. The use of PCSA weights allows us to compare the activation of different muscles and sum them accordingly, which provides a more comprehensive measure of muscular effort.

Interaction torque

The human–exoskeleton interaction torque is estimated based on Eq. 1, given by

$$\boldsymbol{u}_{int} = \boldsymbol{\Gamma}(\gamma, \dot{\gamma}, \ddot{\gamma}, \boldsymbol{a}, \boldsymbol{q}, \dot{\boldsymbol{q}}, \ddot{\boldsymbol{q}}) - \boldsymbol{u}_E. \tag{4}$$

The mean absolute interaction torque is then calculated for each joint as:

$$\tau_{j,s} = \frac{1}{T_s} \int_{T_s} \left| u_{int,j}(t) \right| dt,$$

where $j \in \{$hip$_{right}$, knee$_{right}$, hip$_{left}$, knee$_{left}\}$ is the joint index. The overall absolute interaction torque with each controller is computed as

$$\tau_{c,v,j} = \sum_{s \in S_{c,v}} T_s \tau_{j,s}.$$

The total interaction torque ($\tau_{c,v}^{tot}$) is finally obtained for each controller as the average interaction torque across all joints.

VO2

VO2 is computed for each breath. To normalize the VO2 measurements across participants, the average VO2 during treadmill walking with no exoskeleton at each speed v is computed as:

$$\bar{\eta}_v = \underset{n \in Nv}{\text{mean}} \eta_n,$$

where n is the breath index and N_v is the set of all breaths during walking with no exoskeleton at treadmill speed v. The normalized VO2 during exoskeleton walking is then computed as

$$\hat{\eta}_{c,v,n} = \{\eta_n / \bar{\eta}_v | n \in N_{c,v}\},$$

where $N_{c,v}$ is the set of all breaths during walking with the exoskeleton at treadmill speed v with controller c. The first five breaths after a treadmill or controller switch are excluded to eliminate the transition effect on metabolic rate due to cardiovascular system adjustment. The number of excluded steps is chosen based on the experiment design, where the treadmill speed started from ultra-slow (0.4 m/s) and increased in two steps. Given that our cardiovascular system reacts faster in case of speed increase compared to speed decrease, we expected to observe faster transitions in the collected metabolic rate, which was verified as shown in Fig. 5. The sum of the VO2 measurements is also obtained for all of the exhales for each controller as

$$\hat{\eta}_{c,v}^{tot} = \sum_{n \in N_{c,v}} \hat{\eta}_{c,v,n}.$$

Human–exoskeleton interaction portrait (IP) analysis

To examine the impact of each controller on the human–exoskeleton interaction dynamics, we analyzed the changes in total interaction torques ($\Delta\tau$) relative to variations in total muscular effort ($\Delta\mu$) when switching from controller c_1 to controller c_2 ($c_1 \rightarrow c_2$). For each treadmill speed (v), these changes are computed as:

$$\begin{aligned} {}_{c_1}^{c_2}\Delta\tau_v^{tot} &= \tau_{c_2,v}^{tot} - \tau_{c_1,v}^{tot} \\ {}_{c_1}^{c_2}\Delta\mu_v^{tot} &= \mu_{c_2,v}^{tot} - \mu_{c_1,v}^{tot}. \end{aligned}$$

After max-normalization of $\Delta\tau$ and $\Delta\mu$ across all strides of each walking speed, controller, participant, separately, we compare their variation with respect to each other. Figure 1 illustrates the possible outcomes:

- Disagreement Increase ($\boldsymbol{\Delta\tau > 0}$, $\boldsymbol{\Delta\mu > 0}$) This condition is associated with an increase in both the total interaction torque and the total muscular effort, indicating that switching from controller c_1 to controller c_2 has led to an elevation of human muscular effort. Consequently, their contribution to motion has increased. This, however, has resulted in a higher total interaction torque with the exoskeleton, implying that the applied torques by the exoskeleton are

not aligned with the user's desired motion. As a result, the user needs to exert additional effort to correct the motion while contending against the applied torques from the exoskeleton. Thus, the increased interaction indicates a lack of harmony between the user's intentions and the assistance delivered by the exoskeleton.

- Disagreement Decrease ($\Delta\tau < 0$, $\Delta\mu < 0$) If controller c_2 demonstrates improved consistency compared to c_1 with the user's desired motion, the user will experience less resistance from the exoskeleton. This reduced discordance between the exoskeleton and the user's intended movements results in decreased total muscular effort and overall exertion by the user.

- Human Yields Control to Robot ($\Delta\tau > 0$, $\Delta\mu < 0$) In this case the user may relinquish motion control to the exoskeleton reducing their voluntary contribution to the gait demonstrated by lower muscular effort. Consequently, the exoskeleton must generate the necessary torque to facilitate the movement of both the exoskeleton and the passive dynamics of the human body. The increase in human–exoskeleton interaction torques, in this scenario, is not due to conflicts between the exoskeleton's motion and the user's desired motion but rather because the exoskeleton is effectively carrying the user's body.

- Human Takes Control ($\Delta\tau < 0$, $\Delta\mu > 0$) In a contrasting scenario, the exoskeleton may encourage the user's active participation in the motion, resulting in an increased level of muscular effort. Consequently, the total interaction torque between the user and the exoskeleton may decrease. This reduction occurs because the human and exoskeleton motions are synchronized in time and consistent in space, creating a harmonious alignment between the two.

We conducted the aforementioned analysis at various speeds for the TBC→HTC, TBC→AMTC, and HTC→AMTC cases. We also performed a stride-wise analysis for the TBC→HTC and TBC→AMTC scenarios, which involves computing changes of total interaction torque and muscle effort at each stride during the HTC and AMTC controllers as

$$_{TBC}{}^c \Delta\mu_{v,s} = \mu_{c,v,s} - \mu_{TBC,v}^{tot}$$
$$_{TBC}{}^c \Delta\tau_{v,s} = \tau_{c,v,s} - \tau_{TBC,v}^{tot},$$

where $c \in \{\text{HTC, AMTC}\}$. These calculations allowed us to analyze the precise changes in interaction force and muscular effort for each stride during the HTC and AMTC controllers in relation to the TBC controller. For

the sake of illustration, $\Delta\tau$ and $\Delta\mu$ are graphed in polar coordinate normalized to unit circle.

Interaction portrait is a relative measure that compares human adaptation under different control strategies. If a baseline value is provided by a physical therapist or a reference controller, this metric can evaluate individual controllers. Additionally, interaction portrait offers clinicians an abstract metric that quantifies human–exoskeleton interaction during a gait cycle, allowing objective tuning of the exoskeleton assistance strategy.

Statistical analysis

To identify statistical differences, we first employed a Friedman test with a significance level of 0.05 to test group-level differences. Following the Friedman test, we conducted pairwise comparisons, between the blocks, using the Wilcoxon signed-rank test. To account for multiple comparisons between the three blocks, we applied the Bonferroni correction. Non-parametric tests are used as the normality assumption is rejected using Kolmogorov-Smirnov test ($p < 0.0001$) performed prior to all of the statistical comparisons.

Results

Fig. 4 showcases example signals obtained from a typical participant (Participant #9) during robot-assisted treadmill walking with different controllers. Figure 4A shows the mean absolute interaction torque at the right hip joint (as one of the four joints we computed interaction torque about) for each stride. The interaction torque increases with an increase in treadmill speed across all blocks. During walking at 0.4 and 0.6 m/s, AMTC interaction torques are smaller than those of HTC and TBC. Figure 4B shows GM activation ($\mu_{c,v,m}$), selected for visualization here as an example from seven muscles recorded on each leg, for each stride. Similar to the interaction torques, muscular effort increases at higher treadmill speeds, mostly during the HTC and TBC blocks. In the AMTC block, however, GM's muscular effort does not change from 0.6 to 0.8 m/s speeds. Moreover, the muscular effort is smaller during the AMTC block compared to the two other blocks. The relative oxygen uptake ($\eta_{c,v}$) during the experiment for breath cycles is presented in Fig. 4C. As anticipated, the oxygen uptake increases with an increase in treadmill speed in the HTC, AMTC, and TBC blocks. See Fig. 10 for further data on this participant.

An interesting observation in Fig. 4 is the variation in metrics associated with the TBC controller. For instance, Participant #9 experienced varying interaction torques during walking at 0.4 and 0.6 m/s, as shown in Fig. 4A. Conversely, during walking at 0.8 m/s, the variation in
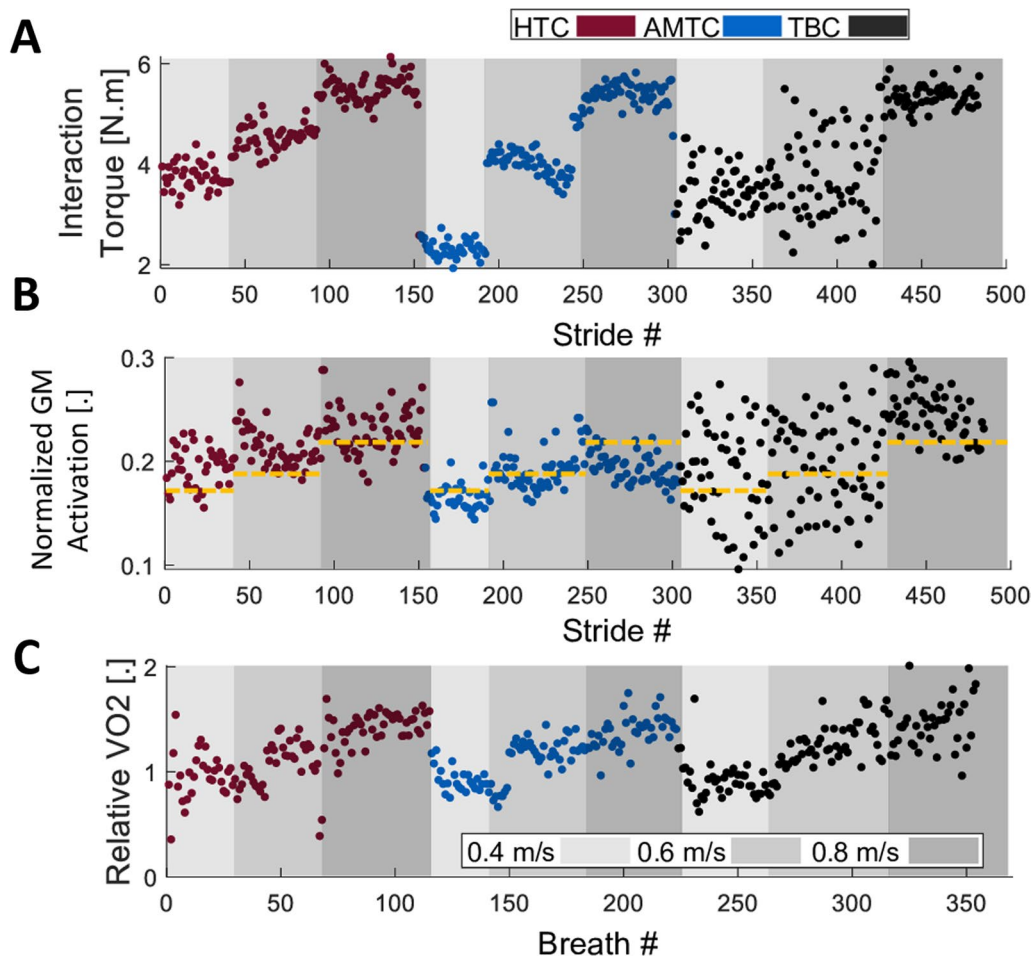
Fig. 4 Examples of a typical participant's (#9) experimental data; for ease of visualization and interpretation, only the interaction torque at the right hip and activation of one of the muscles are illustrated here along with the relative oxygen uptake. **A** The mean absolute interaction torque at the right hip at each stride with each controller and speed for Participant #9. **B** Normal muscle activation for the Gastrocnemius Medialis (GM) at the right leg. The dashed line represents average activation during no-exoskeleton walking. GM was chosen since it showed the strongest sensitivity to changes in the controller. **C** Relative oxygen uptake with respect to no exoskeleton walking for each breath for each controller and speed. The oxygen uptake has increased with the increase in treadmill speed

the interaction torque decreases, demonstrating a more consistent performance by the participant. A similar observation is evident in the case of GM muscle activation (Fig. 4B). For further investigation, Fig. 5 illustrates the average profile of GM activation and hip interaction torque, temporally normalized with respect to the gait phase during walking at 0.4, 0.6, and 0.8 m/s. Both metrics exhibit a large standard deviation (shaded area) during walking at 0.4 and 0.6 m/s, while the standard deviation significantly drops during walking at 0.8 m/s. This indicates an inconsistency in the participant's performance in both spatial and temporal aspects.

Overall performance analysis
Figure 6A shows the sum of the oxygen uptake for all participants for each of the TBC, HTC, and AMTC blocks

during walking at 0.4, 0.6, and 0.8 m/s. TBC and AMTC have the highest and lowest metabolic rate at all walking speeds, respectively. The AMTC-resultant metabolic rate is significantly less than other controllers, at 0.4 and 0.6 m/s speeds, where AMTC resulted in $22.9\% \pm 17.1$ (Friedman: $p < 0.05$, Wilcoxon signed rank: $p_{TBC,AMTC} < 0.01$) and $28.7\% \pm 12.7$ (Friedman: $p < 0.01$, Wilcoxon signed rank: $p_{TBC,AMTC} < 0.01$) decrease in the total oxygen uptake, respectively, compared to TBC. The total mean absolute interaction torque is similarly illustrated for the participants in Fig. 6B. AMTC has the lowest interaction torque compared to TBC and HTC, indicating the least disagreement between the exoskeleton assistance and the user's desired motion. With respect to the TBC, AMTC shows $17.1 \pm 12.5\%$, $12 \pm 15\%$, and $9.2 \pm 7.7\%$ reduction in human–exoskeleton total interaction during walking at
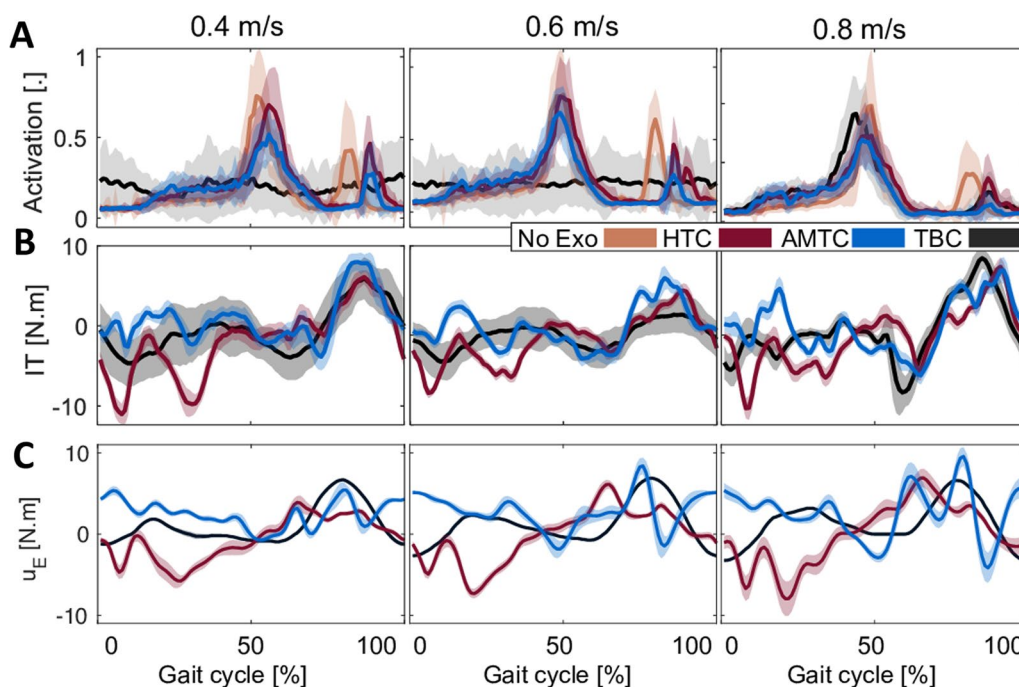
Fig. 5 Muscle activation, interaction torque, and exoskeleton applied torque profiles with respect to the gait phase for participant #9. **A** The average normalized muscle activation pattern for the TBC, HTC, and AMTC blocks for the right Gastrocnemius Medialis during walking at 0.4, 0.6, and 0.8 m/s. The shaded area represents the standard deviation of the muscle activation about their mean value. Similarly, the average human–exoskeleton interaction torque and exoskeleton joint torques at the right hip are plotted in **B** and **C**, respectively
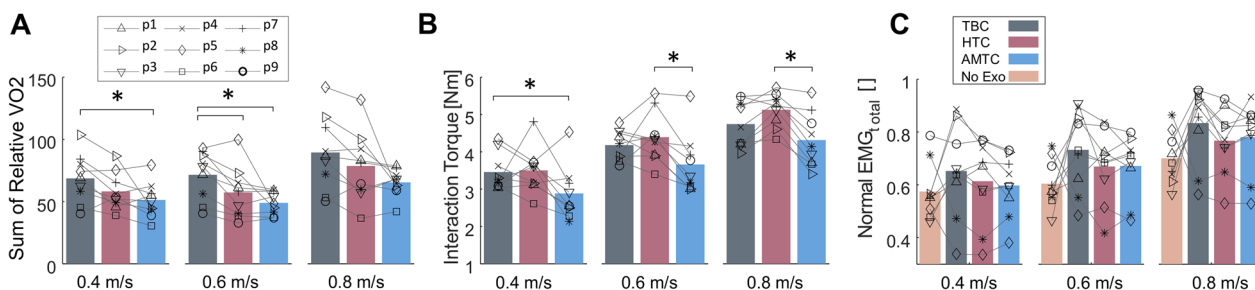
Fig. 6 The average performance metrics for each treadmill speed and controller across participants. **A** The sum of the relative oxygen uptake across all the strides for each speed in each controller block graphed for each participant. The bars show the average of the sum of the oxygen uptake across all participants. Similarly, the average total absolute value of the human–exoskeleton interaction and total normalized muscle effort are graphed in **B** and **C**, respectively. Asterisks indicate statistical difference between the median of the compared populations

0.4, 0.6, and 0.8 m/s speeds, respectively. The difference is statistically significant at 0.4 m/s walking (Friedman: $p < 0.05$, Wilcoxon signed rank: $p_{TBC,AMTC} < 0.01$). Compared to HTC, AMTC shows $19.8 \pm 21.1\%$, $17.9 \pm 10.1\%$, and $18.1 \pm 9.9\%$ reduction in human–exoskeleton total interaction. These differences are statistically significant in the case of walking at 0.6 m/s (Friedman: $p < 0.05$, Wilcoxon signed rank: $p_{HTC,AMTC} < 0.004$) and 0.8 m/s (Friedman: $p < 0.001$, Wilcoxon signed rank: $p_{HTC,AMTC} < 0.01$) walking.

Figure 6C shows the total muscle effort for participants' right legs during walking at 0.4, 0.6, and 0.8 m/s across the three different controllers. Natural walking without the exoskeleton has the lowest total muscle effort compared to other cases in which the exoskeleton is involved. This is expected as wearing the exoskeleton adds about 17 kg of extra weight to the body resulting in higher muscle effort. Among the three controllers, TBC has the highest total muscular effort at all speeds. AMTC and HTC's total muscular effort are close in all cases while

AMTC is slightly lower and higher during walking at 0.4 and 0.6 m/s, respectively. None of the identified differences are statistically significant (Friedman: $p_{v=0.4} = 0.506$, $p_{v=0.6} = p_{v=0.8} = 0.057$). Further results in regard to the comparisons of ground reaction force and gait spatiotemporal metrics with each of the controllers are discussed in subsection B.2.

Interaction portrait analysis

Figure 7 compares the examined controllers one by one during walking at 0.4, 0.6, and 0.8 m/s by illustrating the average change in the max-normalized total muscular effort with respect to the change in the max-normalized total interaction torque (the average IP is plotted by a single vector for each participant). To compare
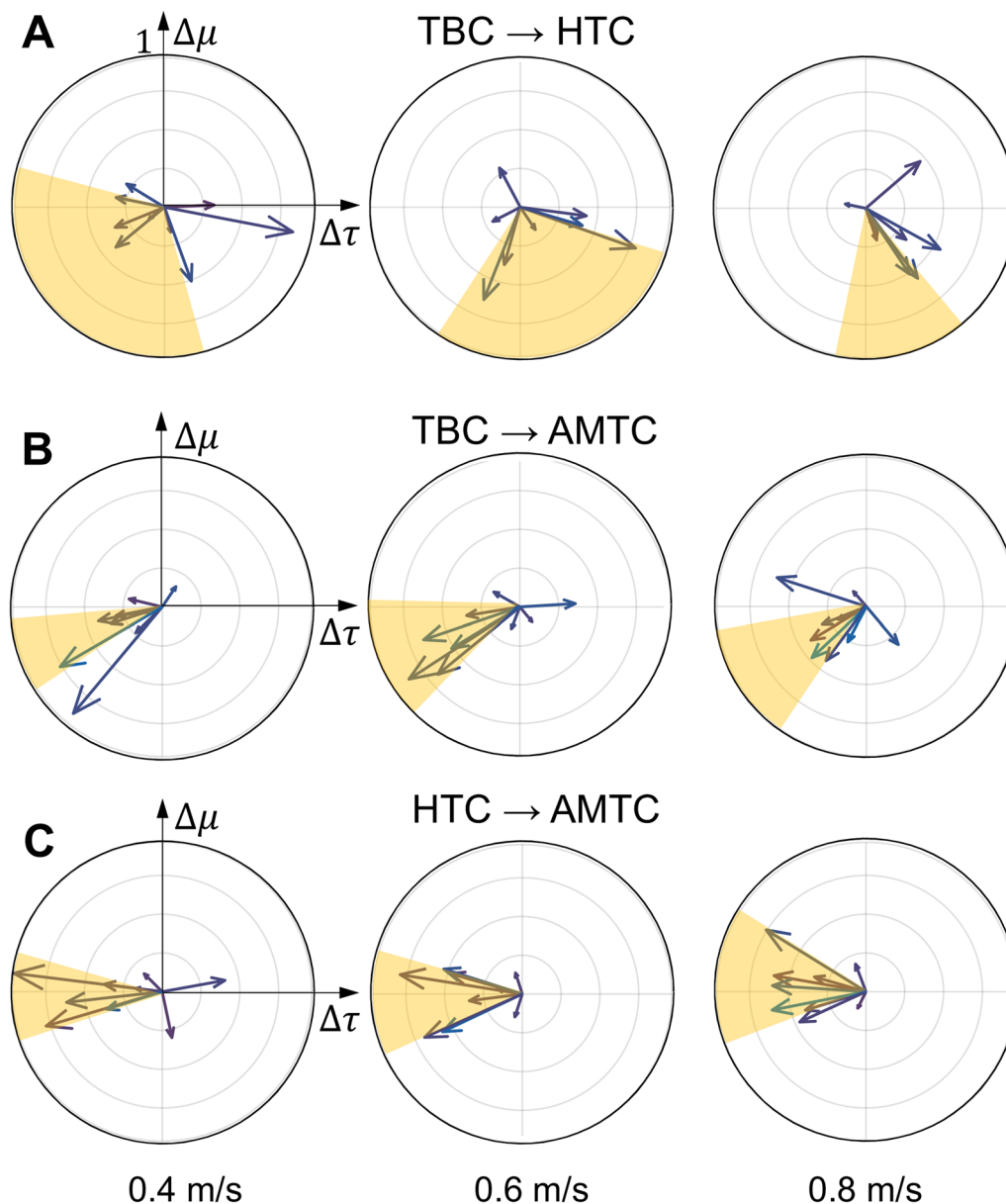
Fig. 7 Comparing the average interaction portrait for each pair of controllers. The average interaction portrait (IP) depicted according to the average total muscle effort and the average total human–exoskeleton interaction for each participant computed at each of the 0.4, 0.6, and 0.8 m/s speeds for the TBC→HTC, TBC→AMTC, and HTC→AMTC illustrated in **A**, **B**, and **C**, respectively. The yellow areas denote the area between 25 and 75 percentiles

the IP results of participants more easily, Fig. 7A shows the average IP for HTC compared to TBC, denoted as $[^{HTC}_{TBC}\Delta\tau_\nu^{tot}, ^{HTC}_{TBC}\Delta\mu_\nu^{tot}]$. During walking at 0.4 and 0.6 m/s, participants adapt differently to HTC compared to TBC, as the average IP vectors are spread in all quadrants. During walking at 0.8 m/s, however, the majority of average IP vectors fall within the fourth quadrant, indicating that most participants yield control to the HTC-controlled exoskeleton. This observation aligns with participants exhibiting the lowest total muscular effort when walking with an HTC-controlled exoskeleton, as shown in Fig. 6C. Similarly, Fig. 7B presents the average IP vectors of AMTC compared to TBC, denoted by $[^{AMTC}_{TBC}\Delta\tau_\nu^{tot}, ^{AMTC}_{TBC}\Delta\mu_\nu^{tot}]$. Unlike HTC, AMTC effectively decreases user-exoskeleton disagreement at all tested speeds, as indicated by the majority of average IP vectors concentrated in the third quadrant. To further examine, Fig. 7C compares the HTC and AMTC controllers, denoted as $[^{AMTC}_{HTC}\Delta\tau_\nu^{tot}, ^{AMTC}_{HTC}\Delta\mu_\nu^{tot}]$. It shows that compared to HTC, participants lean more toward contributing to the motion rather than yielding control to the exoskeleton with AMTC, as most of the average IP vectors fall around the border of the second and third quadrants at all three speeds.

Individual adaptation strategy

We analyzed the dependency of user adaptation strategy formed in interaction with each of the HTC and AMTC cases with respect to the TBC. To this end, we first computed the average total muscular effort and interaction torque in TBC. We then computed the total muscular effort and interaction torque for each stride in the HTC and AMTC cases. For each stride, the difference in total muscle effort and interaction torque is then computed with respect to the TBC. Figure 8 shows the stride-wise IP distribution of the TBC→HTC ($[^{HTC}_{TBC}\Delta\tau_{\nu,s}, ^{HTC}_{TBC}\Delta\mu_{\nu,s}]$ in red), and TBC→AMTC ($[^{AMTC}_{TBC}\Delta\tau_{\nu,s}, ^{AMTC}_{TBC}\Delta\mu_{\nu,s}]$ in blue) for each participant separately during walking at 0.8 m/s. The graphs are ordered from left to right and top to bottom, corresponding to a monotonic increase in participants' body mass. According to the graph, except for participant #9, our lighter participants leaned towards contributing more to the gait and leading the motion, with either HTC or AMTC, as their IP is consistently distributed in the third quadrant. On the other hand, heavier participants in our experiment tended to relinquish control and passively follow the exoskeleton. This behaviour was particularly noticeable in the two heaviest participants, who consistently adopted this strategy with the HTC, resulting in their IP distribution falling in the fourth quadrant. In contrast, their IP distribution for the AMTC was more widely spread.

The strength of the adopted co-adaptation strategy is proportional to the IP radial distribution. Accordingly, the higher radial coordinates distribution of TBC→ AMTC compared to TBC→HTC for participants #2, 3, 4, and 5 reveals that AMTC-controlled exoskeleton led users to adopt a more consistent strategy compared to the HTC case. Participants #8 and 9, as exceptions, adopted a more consistent strategy during HTC. Figure 8 also reveals that Participant #9 did not adopt a strong strategy in either the HTC or AMTC cases.

Discussion
Human adaptation

The interaction torques and GM muscle activity during walking with TBC exhibited different variations across walking speeds (as shown for a typical participant); with higher variations during 0.4 and 0.6 m/s and lower variations during 0.8 m/s. The inherent difference between the TBC and the other two controllers can explain this observation. During the TBC block, the feedforward torque is generated regardless of the user's performance, and the exoskeleton has no capacity for adapting to the user. Therefore, it is entirely up to the user to adapt to the torque delivered by the exoskeleton. During walking at 0.4 and 0.6 m/s, Participant #9 was unable to adjust their gait timing to the exoskeleton, resulting in inconsistent interaction with the exoskeleton. At the higher speed, however, this user was able to synchronize their gait with the exoskeleton assistance and, therefore, adopted a solid interaction strategy, which emerged with a lower variation in all the above metrics. This has not been the case for all participants, as six of them were not successful in effectively synchronizing their walking to the TBC-controlled exoskeleton at any speed. These results highlight the importance of human–robot co-adaptation, which is not achievable with a time-based controller. TBC, a controller with a non-zero interaction torque, was selected as the baseline rather than a passive or transparent controller, as it allows us to fully utilize the capacity of the IP analysis. With a passive exoskeleton as a baseline, the user has the burden of moving the inertia of the robot, resulting in increased muscular effort, influencing their adopted strategy. In turn, any well-designed assistive controller is expected to result in an IP which falls only in quadrants 3 and 4 if compared to a passive exoskeleton. Conversely, a transparent controller eliminates physical interaction, making it less suitable as a baseline for comparison. It can be seen that any assistive controller would result in IP values that fall in the right-hand-side quadrants when compared to a transparent controller as a baseline. As presented in Fig. 9, some participants were able to adjust their timing with the TBC and benefit from
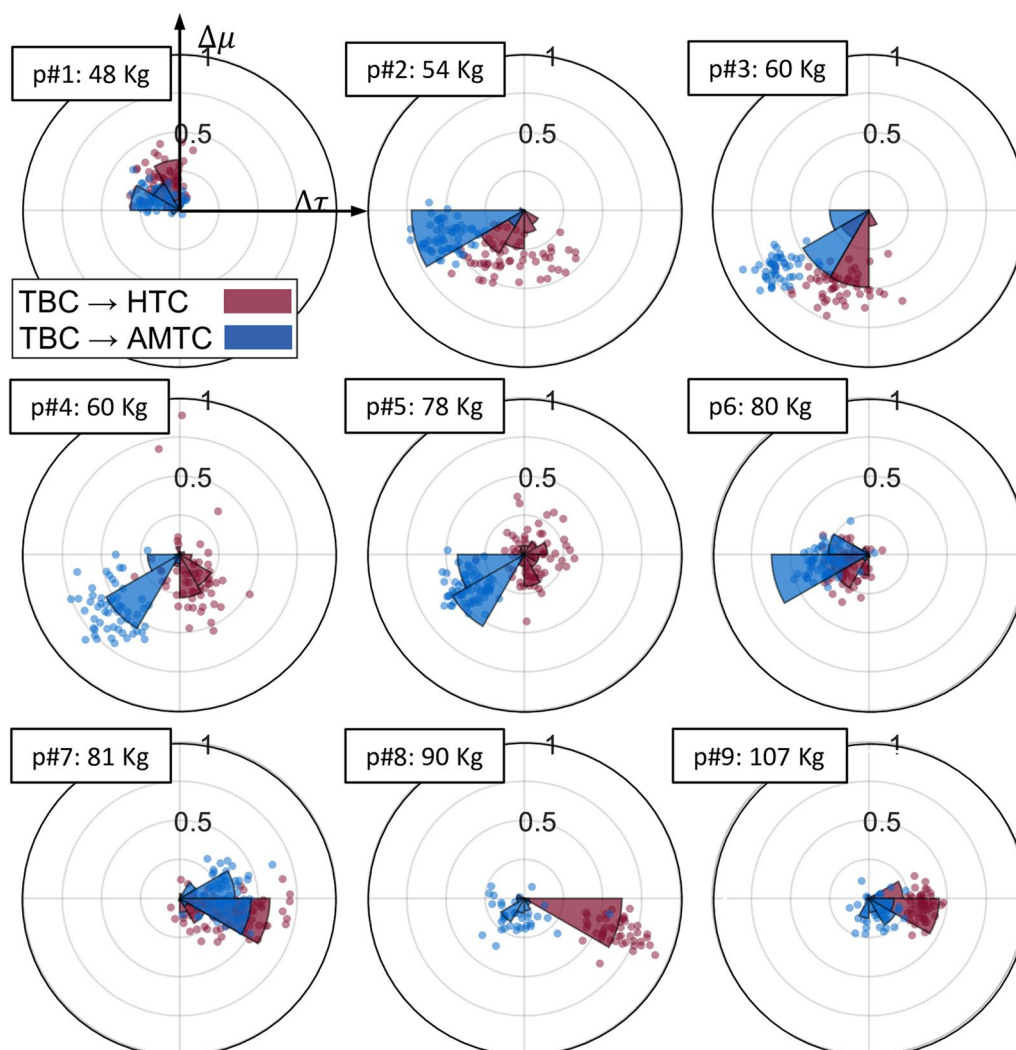
Fig. 8 Interaction portrait distribution along with their polar histogram for HTC and AMTC blocks with respect to the average total muscle effort and total interaction torque across all strides during the TBC block graphed for each participant plotted for walking at 0.8 m/s. The radial coordinate of data points is normalized with respect to the maximum radius computed across all participants' strides. Participants are arranged increasingly according to their body mass. The polar histograms show the concentration intensity of the depicted points. Each bin of the histogram covers $\pi/6$ rad

its assistance, allowing users to decrease their muscular effort. This behaviour would not be exhibited in the case of walking with passive or transparent exoskeleton control. Moreover, we intentionally implemented no adaptation capacity in the TBC to keep everything fixed and allow users to adapt themselves to a fully predictable assistance.

Additionally, in this study, we did not calibrate the torque of controllers with each participant's body mass. This was avoided mainly to maintain a similar range of torques for all three controllers and to keep the comparison fair. Such calibrations, which is inherent to HTC, can provide more personalized torques and affect the user

interaction strategy which can be studied using IP in the future.

Importance of IP analysis

In Fig. 6, the lower total muscular effort during walking with the HTC and AMTC compared to TBC is consistent with their lower metabolic rate with respect to the TBC, indicating that both controllers reduce the walking effort more than the TBC-controlled exoskeleton. Muscular effort has been previously used to assess walking efficiency and user engagement. The main shortcoming of such analysis is that it is blind to the physical interaction between the user and the exoskeleton. For instance, the
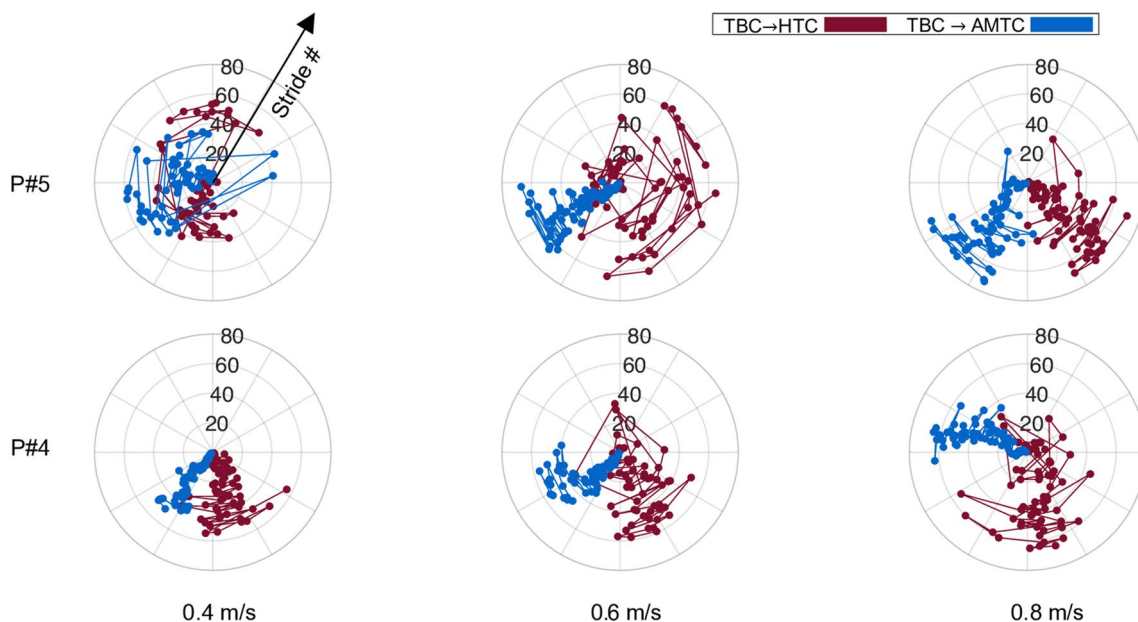
Fig. 9 Evolution of IP phase at each stride at different walking speeds for two sample participants. The top and bottom rows depict IP phase evolution during walking at 0.4, 0.6, and 0.8 m/s for each of the TBC→HTC and TBC→AMTC cases for participants #5 and #4, respectively

decrease in muscular effort, which has often been used as an indicator of improved gait [5], may be due to the user relying fully on the exoskeleton and lack of engagement in motor tasks. The increase or maintenance of certain levels of muscular effort alone could be difficult to interpret, as it may be due to user engagement or disagreement between the user and the exoskeleton. IP analysis is an effort to remove such ambiguity by joint analysis of muscular effort and interaction torque. According to Fig. 6B, HTC resulted in higher interaction torque compared to the TBC. This indicates that even though HTC and AMTC both reduced users' metabolic rate and muscular effort, they encouraged users to adopt two different interaction strategies. IP analysis in Fig. 7 reveals that with the HTC controller, users relinquished control to the exoskeleton, passively following the exoskeleton's motion. In contrast, AMTC encouraged users to lead the motion more actively. Our IP analysis suggests that the HTC controller is particularly well-suited for applications requiring human augmentation, such as in industrial settings for workers or healthcare environments for nurses. In these contexts, the primary goal is to minimize human exertion, thereby enhancing operational capabilities and safety [40]. Conversely, the AMTC controller shows greater promise in rehabilitation contexts for individuals with residual motor functions, such as those with incomplete spinal cord injuries or post-stroke conditions. Here, the imperative is to actively involve the user in task execution, thereby amplifying their motor functions and accelerating the recovery processes [41].

Figure 7 also demonstrates that different participants adopted a more consistent strategy with AMTC compared to the HTC, as the average IP vectors across participants exhibit lower variation with AMTC compared to the HTC controller.

IP distribution itself can also shed light on the strength of the adopted strategy in each participant depending on the IP radial coordinate. This is more evident in Fig. 8 where each point of IP represents the difference in muscle effort and interaction torque obtained for each stride. As an example, the IP analysis in Fig. 8 reveals that Participant #4 (2nd row, 1st column) and Participant #5 (2nd row, 2nd column) adopted the same interaction strategy with the AMTC controller compared to the TBC. This is, nevertheless, more significant for Participant #4 due to the larger radial coordinates of the distributed points compared to those of Participant #5.

Using the IP analysis, it is also possible to track the evolution of the adopted strategy across strides at each walking speed. Figure 9, as an example, shows the evolution of the IP phase for each of the TBC→HTC and TBC→AMTC comparisons for participants #5 and #4, respectively. As the angular coordinate of IP shows the essence of the adopted strategy, its variation is an indicator of how consistent that strategy is. Therefore, implied by the large variation in the IP phase, Participant #5 converged to a consistent interaction strategy with neither the HTC nor AMTC controllers during 0.4 m/s walking. Assuming a dynamic primitive framework for human movement control, ultra-slow walking may lead to very different walking

patterns and interaction with the exoskeleton due to possible limitations of the human dynamic primitives and movement segmentation [42–45]. The difficulty in maintaining smoothness and continuity, therefore, explains the lack of convergence to a consistent interaction with the exoskeleton while walking at 0.4 m/s. During walking at 0.6 m/s, however, the user adopted a more consistent strategy using AMTC, evidenced by low variations in the IP phase. In the case of the HTC controller, the participant's strategy remained inconsistent. It was only during walking at 0.8 m/s that Participant #5 was able to converge to consistent interaction strategies both with the AMTC and the HTC controllers. Our IP analysis, in this case, shows that AMTC decreased the human–exoskeleton interaction, but the user did not completely obtain the motion control or yield the motion to the exoskeleton, as the IP phase is still in the third quadrant. In the case of the HTC controller, the user has relied more on the exoskeleton assistance since the IP phase is primarily concentrated in the 4th quadrant. Participant #4, in contrast to Participant #5, converged to a consistent interaction with the exoskeleton at all three walking speeds. The HTC controller, regardless of the walking speed, has guided the participant to rely more on the exoskeleton as the IP phase is mostly concentrated on the border of the 3rd and 4th quadrants. In the case of the AMTC controller, however, we observe that as the gait speed increases, the user strategy develops more toward leading the gait and contributing to motion control, evidenced by an 83-degree shift in the average IP phase during walking at 0.8 m/s compared to 0.4 m/s.

These results showcased the ability of IP analysis to provide an objective comparison of different exoskeleton controllers, the adopted interaction strategy by the user, as well as evaluation of user-exoskeleton co-adaptation. Besides offline analysis, IP addresses the lack of a quantitative metric to demonstrate human interaction with exoskeletons in a human-in-the-loop framework. It provides designers with an easily embeddable metric to tailor the exoskeleton controller to the unique requirements of each application or participant [46].

IP focuses on the co-analysis of muscle activity and interaction torque to evaluate human–exoskeleton interaction. While it does not directly provide information on kinematics, it offers a unique perspective on the roles of the user and exoskeleton, as well as their co-adaptation strategies, which are not easily discernible through traditional kinematic analysis alone. In the context of individuals with motor impairments, distinguishing the user's possible compensatory strategies from the intended exercises is crucial [47, 48]. This can be achieved through kinematic and electromyography analyses. IP analysis can complement kinematic analyses by providing insights

into how each user responds to different assistive controllers and alters their muscle activity and interaction torque over time, which can be indicative of their engagement in motor control. For example, integrating IP analysis with kinematic analyses similar to the approach used by Ishmael et al. [49], where biological residual torque was estimated using inverse dynamics to understand the torque required for specific movements, can offer a more comprehensive understanding of patient interaction with the exoskeleton. Kinematic data can provide detailed information on joint angles and movement patterns, and IP can offer insights into the underlying muscle activity and interaction forces that drive these movements. This combined approach can help identify assistive control strategies more effectively and provide a holistic view of patient-exoskeleton interaction, ultimately leading to better customization of exoskeleton control strategies to meet each individual's needs.

It is also notable that, user physical interaction and muscular effort under the baseline controller were averaged across gait cycles. For each step of the tested controllers, the distance from these means was calculated to obtain the IP distributions. If the baseline controller measurements are skewed, a Bayesian approach or Mahalanobis distance could offer a more accurate comparison. Moreover, to compute IP points, we abstracted each stride's information into a single quantity while user strategy may be different alongside the gait phase. For example, the user may prefer to rely on the exoskeleton only during the swing phase while leading the motion during the stance phase. Extensions, such as separate IPs for stance and swing phase, can be easily computed in future if needed for analysis and decision making of the designers and physical therapists.

Conclusion

We proposed a new metric for the analysis of human–exoskeleton interaction (interaction portrait) and employed it in investigating the effect of three feedforward controllers in enhancing human–exoskeleton interaction during assisted treadmill walking at different speeds. Through interaction portrait analysis, we found that the HTC controller demonstrated a more suitable performance for human augmentation along with reducing muscle activation and metabolic cost. On the other hand, the AMTC controller, also proposed in this study, proved to be more suitable for rehabilitation applications, as it promoted user reliance on their own muscular capacity by making the exoskeleton transparent.

Furthermore, we observed that the human adaptation pattern facing each of the HTC and AMTC controllers was influenced by the participants' weight. Individuals with lower weight tended to take control with the

AMTC controller, while heavier participants were more inclined to relinquish control when interacting with the HTC-controlled exoskeleton. IP analysis has been only performed to evaluate the able-bodied individuals' interaction with exoskeletons. As the next step of this research, we plan to analyze the interaction portrait of motor-impaired individuals with exoskeletons equipped with different assist-as-needed controllers to provide a meaningful and objective comparison of these controllers. Developing a probabilistic framework for interaction portrait analysis, considering interaction power instead of interaction torque are considered as future directions of this work.

Appendices

Appendix A: complementary example data

Figure 10A illustrates the modifications made to the hip reference trajectory (Δr_{hip}) during the AMTC block. These modifications occur after the HTC block and before the TBC block, as depicted in (Fig. 3B), across 0.4, 0.6, and 0.8 m/s walking speeds. Similarly, Fig. 10B showcases the adaptation of the Fourier coefficients (θ) and their convergence pattern during the AMTC block during walking at 0.4 m/s. The Fourier coefficients begin to adapt as soon as that block starts. It takes approximately 20 s for them to converge, and they subsequently exhibit minor oscillations around their converged values until

the treadmill speed is switched to 0.6 m/s. This change in treadmill speed induces new walking conditions, resulting in distinct gait patterns. Consequently, the Fourier coefficients converge toward a new set of steady-state values. A similar pattern emerges when the treadmill speed is switched to 0.8 m/s. Pearson correlation between the vertical Ground Reaction Forces during each of the HTC, AMTC, and TBC blocks and natural walking with no exoskeleton is plotted for each stride in Fig. 10C. According to the graph, the GRF patterns resemble the GRF during natural walking at 0.6 and 0.8 m/s. During walking at 0.4 m/s, however, the correlation slightly decreases in all three blocks. Finally, Fig. 10D shows the computed stride length. As expected, in all three blocks, the stride length increases with the increase in treadmill speed.

Appendix B: comparison with natural walking

To identify which controller led to a gait closer to natural walking, we analyzed the spatiotemporal parameters of gait (obtained using GaitUp Sensors) in TBC, HTC, and AMTC and compared them to those of each participant's natural walking with no exoskeleton. Moreover, we analyzed the correlation of recorded ground reaction torques in the case of each controller with natural walking.

Gait spatiotemporal parameters

Figure 11A shows the maximum heel clearance in natural walking condition (with no exoskeleton) and during exoskeleton walking at each of the TBC, HTC, and
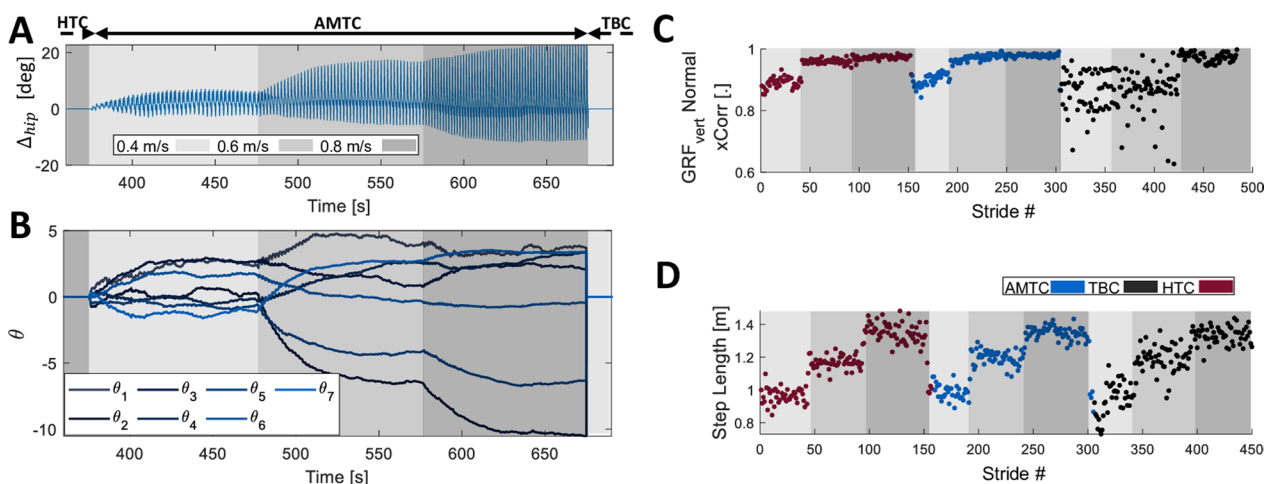
Fig. 10 **A** Evolution of the modification term for Participant #9's right hip trajectory (Δ_{hip}). Δ_{hip} is zero before and after the AMTC block. During the AMTC block, the modification term of the trajectory adapts to make the reference trajectory closer to the user joint angle. At each walking speed, the modification pattern in the steady state converges to a different amplitude and shape, indicating that the user joint angle, and as a result, the exoskeleton reference trajectory has evolved to a different pattern at each speed. **B** Modification trajectory coefficients evolve during the AMTC block. Each coefficient converged to a steady state value at the end of each treadmill speed condition. After the change in treadmill speed, coefficients converge to new optimum levels. These levels, as mentioned for the modification term of the hip trajectory, differ for each speed. **C** Pearson correlation between the GRF of each stride with the average GRF profile recorded during natural walking without the exoskeleton. **D** Stride length was computed using the Physiolog 6 s IMU sensors
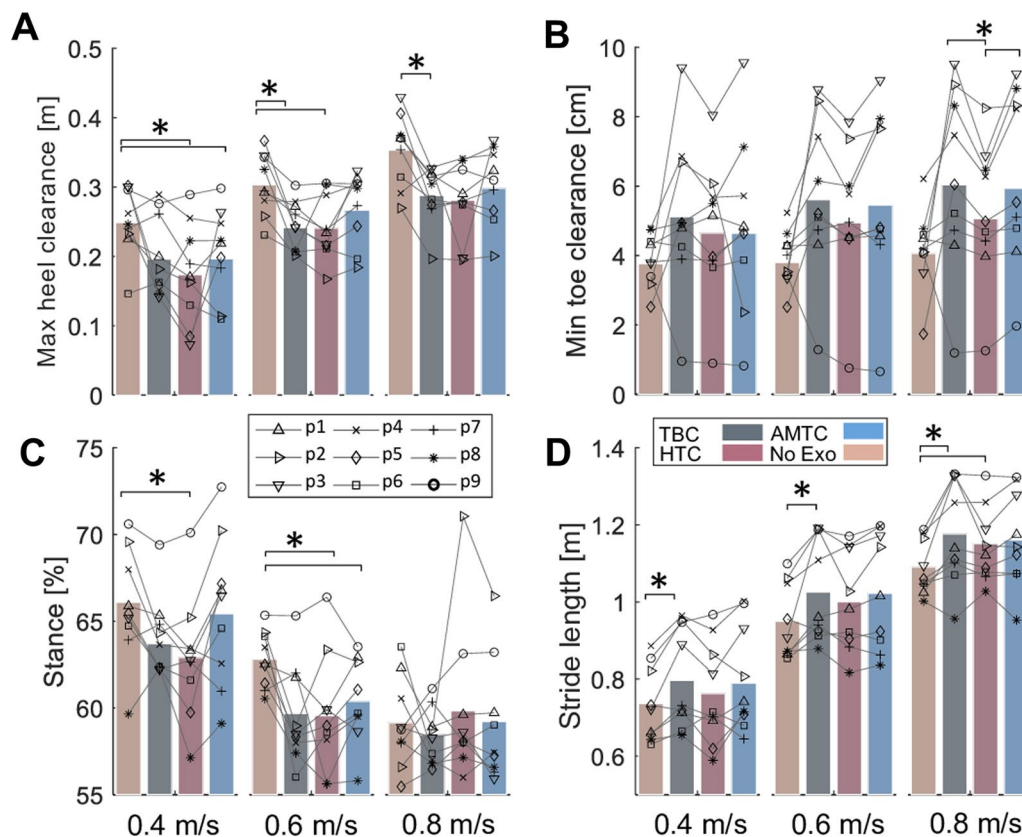
Fig. 11 The average maximum heel clearance (**A**), minimum toe clearance (**B**), stance percentage (**C**), and stride length (**D**), computed for each of the 0.4, 0.6, and 0.8 m/s speeds during natural walking with no exoskeleton, TBC, HTC, and the AMTC blocks for each participant. Bars show the average of each metric across participants. Asterisks indicate statistical difference between the median of the compared populations

AMTC blocks at 0.4, 0.6, and 0.8 m/s speeds. Natural walking has the greatest heel clearance, which is expected as the addition of the exoskeleton weight makes it harder for the participant to lift their foot to their convenient level. Among the three controllers, AMTC has a heel clearance closer to that of natural walking, indicating that maintaining the desired heel clearance is easier for the participant in the case of this controller. Similarly, Fig. 11B compares the minimum toe clearance, showing that at all walking speeds, natural walking with no exoskeleton has the lowest minimum toe clearance. The HTC controller demonstrates lower toe clearance than the TBC and AMTC at all speeds. However, these differences are not statistically significant (Friedman: $p_{v=0.4} = 0.144$, $p_{v=0.6} = 0.061$) unless during walking at 0.8 m/s, where the HTC has led to a 21.3%±18.2 and 12.2%±9.3 decrease in minimum toe clearance compared to the AMTC and TBC, respectively (Friedman: $p < 0.001$, Wilcoxon signed rank: $p_{HTC,AMTC} < 0.01$, $p_{HTC,TBC} < 0.01$).

Regarding the stance percentage, as depicted in Fig. 11C, AMTC exhibits the closest behaviour to natural walking at all speeds. In all cases, TBC has a smaller stance percentage compared to natural walking. During walking at 0.4 and 0.6 m/s, HTC has the smallest stance percentage. During walking at 0.8 m/s, however, HTC has the highest stance percentage. Finally, Fig. 11D illustrates the stride length for each of the controllers at the three experimented walking speeds. The stride length generally increases with the increase in treadmill speed. At each individual speed, however, natural walking appears to have the smallest stride length on average, mostly compared to the TBC, which has the highest stride length (Friedman: $p < 0.05$, Wilcoxon signed rank: $p < 0.01$ for all speeds).

Ground reaction force

Force plates are utilized to measure the ground reaction forces (GRF) in the vertical, lateral, and longitudinal directions. Heel strike events are detected using the
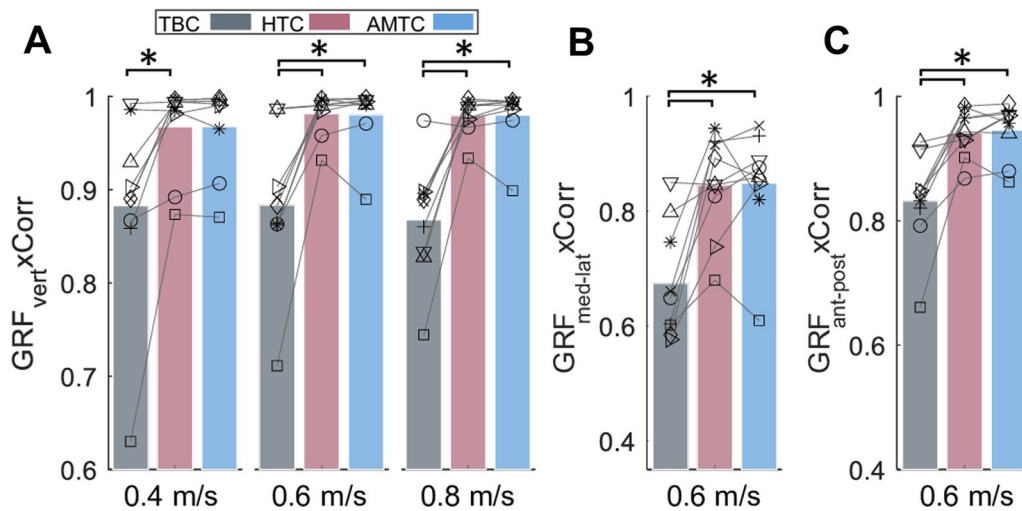
Fig. 12 A The average Pearson correlation computed between the average vertical GRF in natural walking without the exoskeleton and the vertical GRF during walking with each of the proposed controllers at different speeds. The depicted bars show the average of each metric across participants. **B** and **C** shows the similar graph for the mediolateral and antero-posterior GRF plotted only for walking at 0.8 m/s. Astrisks indicate statistical difference between the median of the compared populations

vertical GRF, enabling the segmentation of collected data into individual strides. The recorded GRF during no exoskeleton walking is temporally normalized and averaged based on the gait phase as

$$\bar{f}_v(\phi) = \operatorname*{mean}_{s \in S_v} f_s(\phi),$$

where $v \in \{0.4, 0.6, \text{and } 0.8 \text{ m/s}\}$ is the treadmill speed index, $s \in \mathbb{N}$ is the stride index, S_v is the set of the strides during no exoskeleton walking with speed v, and $f_s(\phi)$ is the temporally normalized GRF at stride s. To assess the similarity between the ground reaction force profiles with each controller and the natural walking without the exoskeleton, a normalized Pearson correlation is computed as

$$\boldsymbol{x}_{c,v,s} = \{\operatorname{Corr}(\boldsymbol{f}_s(\phi), \bar{\boldsymbol{f}}_v(\phi)) | s \in S_{c,v}\},$$

where $S_{c,v}$ is the set of all strides during walking with exoskeleton at treadmill speed v with controller $c \in \{\text{TBC, HTC, AMTC}\}$ excluding the first 10 steps after treadmill or controller switch.

Figure 12A shows the Pearson correlation of the vertical ground reaction force between walking with each of the controllers and natural walking without the exoskeleton. At all speeds, TBC exhibits the most different vertical GRF compared to the other controllers (Friedman: $p_{v=0.4} < 0.05$, $p_{v=0.6} < 0.001$, and $p_{v=0.8} < 0.05$; Wilcoxon signed rank: $p < 0.01$ for all speeds). In contrast to the TBC, HTC and AMTC led to more natural vertical

GRF profiles with Pearson correlations greater than 96% at all speeds. The same observation stands for the GRFs in mediolateral (Fig. 12B) and antero-posterior (Fig. 12C) directions, where TBC shows the least natural GRF profile while HTC and AMTC demonstrate closer to natural walking GRF with Pearson correlations greater than 82.2% and 91.5% in mediolateral and antero-posterior directions, respectively (Friedman: $p < 0.01$; Wilcoxon signed rank: $p < 0.01$ for all cases).

Supplementary Information

The online version contains supplementary material available at https://doi.org/10.1186/s12984-024-01447-1.

Supplementary Material 1

Declarations

References

1. Dupont PE, Nelson BJ, Goldfarb M, Hannaford B, Menciassi A, O'Malley MK, Simaan N, Valdastri P, Yang G-Z. A decade retrospective of medical robotics research from 2010 to 2020. Sci Robot. 2021;6:eabi8017.
2. Duschau-Wicke A, Zitzewitz JV, Caprez A, Lunenburger L, Riener R. Path control: a method for patient-cooperative robot-aided gait rehabilitation. IEEE Trans Neural Syst Rehabil Eng. 2009;18:38–48.
3. Bryan GM, Franks PW, Song S, Reyes R, O'Donovan MP, Gregorczyk KN, Collins SH. Optimized hip-knee-ankle exoskeleton assistance reduces the metabolic cost of walking with worn loads. J Neuroeng Rehabil. 2021;18:1–13.
4. Franks PW, Bryan GM, Martin RM, Reyes R, Lakmazaheri AC, Collins SH. Comparing optimized exoskeleton assistance of the hip, knee, and ankle in single and multi-joint configurations. Wearable Technol. 2021;2:16.
5. Durandau G, Rampeltshammer WF, Kooij H, Sartori M. Neuromechanical model-based adaptive control of bilateral ankle exoskeletons: biological joint torque and electromyogram reduction across walking conditions. IEEE Trans Robot. 2022;38:1380–94.
6. Poggensee KL, Collins SH. How adaptation, training, and customization contribute to benefits from exoskeleton assistance. Sci Robot. 2021;6:eabf1078.
7. Nuckols RW, Lee S, Swaminathan K, Orzel D, Howe RD, Walsh CJ. Individualization of exosuit assistance based on measured muscle dynamics during versatile walking. Sci Robot. 2021;6:eabj1362.
8. Lee UH, Shetty VS, Franks PW, Tan J, Evangelopoulos G, Ha S, Rouse EJ. User preference optimization for control of ankle exoskeletons using sample efficient active learning. Sci Robot. 2023;8:eadg3705.
9. Postol N, Lamond S, Galloway M, Palazzi K, Bivard A, Spratt NJ, Marquez J. The metabolic cost of exercising with a robotic exoskeleton: a comparison of healthy and neurologically impaired people. IEEE Trans Neural Syst Rehabil Eng. 2020;28:3031–9.
10. Witte KA, Fiers P, Sheets-Singer AL, Collins SH. Improving the energy economy of human running with powered and unpowered ankle exoskeleton assistance. Sci Robot. 2020;5:eaay9108.
11. Zhu F, Kern M, Fowkes E, Afzal T, Contreras-Vidal J-L, Francisco GE, Chang S-H. Effects of an exoskeleton-assisted gait training on post-stroke lower-limb muscle coordination. J Neural Engi. 2021;18:046039.
12. Ingraham KA, Remy CD, Rouse EJ. The role of user preference in the customized control of robotic exoskeletons. Sci Robot. 2022;7:eabj3487.
13. Küçüktabak EB, Wen Y, Kim SJ, Short M, Ludvig D, Hargrove L, Perreault E, Lynch K, Pons J. Haptic transparency and interaction force control for a lower-limb exoskeleton. IEEE Trans Robot. 2024.
14. Dalley SA, Hartigan C, Kandilakis C, Farris RJ. Increased walking speed and speed control in exoskeleton enabled gait. 2018 7th IEEE International Conference on Biomedical Robotics and Biomechatronics (Biorob). 2018:689–94.
15. Pisotta I, Tagliamonte NL, Bigioni A, Tamburella F, Lorusso M, Bentivoglio F, Pecoraro I, Argentieri P, Marri F, Zollo L, Molinari M. Pilot testing of a new questionnaire for the assessment of user experience during exoskeleton-assisted walking. 2020.
16. Muijzer-Witteveen H, Sibum N, Dijsseldonk RB, Keijsers NLW, Asseldonk EHF. Questionnaire results of user experiences with wearable exoskeletons and their preferences for sensory feedback. J Neuroeng Rehabil. 2018;15:112.
17. Lee K-S, Lee J, Hwang J. Research trend analysis of usability evaluation in exoskeleton robots. 2022.
18. Nasiri R, Dinovitzer H, Nirosh M, Arami A. Coordinated human-exoskeleton locomotion emerges from regulating virtual energy. PLoS ONE. 2024.
19. Pinto-Fernandez D, Diego T, Carmen Sanchez-Villamanan M, Aller F, Mombaur K, Conti R, Vitiello N, Moreno JC, Pons JL. Performance evaluation of lower limb exoskeletons: a systematic review. IEEE Trans Neural Syst Rehabil Eng. 2020;28:1573–83.
20. Slade P, Kochenderfer MJ, Delp SL, Collins SH. Personalizing exoskeleton assistance while walking in the real world. Nature. 2022;610:277–82.
21. Medina JR, Lorenz T, Hirche S. Synthesizing anticipatory haptic assistance considering human behavior uncertainty. IEEE Trans Robot. 2015;31:180–90.
22. Martinez A, Lawson B, Durrough C, Goldfarb M. A velocity-field-based controller for assisting leg movement during walking with a bilateral hip and knee lower limb exoskeleton. IEEE Trans Robot. 2018;35:307–16.
23. Shushtari M, Nasiri R, Arami A. Online reference trajectory adaptation: a personalized control strategy for lower limb exoskeletons. IEEE Robotics and Autom Lett. 2021;7:128–34.
24. Asl HJ, Yamashita M, Narikiyo T, Kawanishi M. Field-based assist-as-needed control schemes for rehabilitation robots. IEEE/ASME Trans Mechatron. 2020;25:2100–11.
25. Dominijanni G, Pinheiro DL, Pollina L, Orset B, Gini M, Anselmino E, Pierella C, Olivier J, Shokur S, Micera S. Human motor augmentation with an extra robotic arm without functional interference. Sci Robot. 2023;8:eadh1438.
26. Losey DP, Mcdonald CG, Battaglia E, O'Malley M. A review of intent detection, arbitration, and communication aspects of shared control for physical human-robot interaction. Appl Mech Rev. 2018;70:010804. https://doi.org/10.1115/1.4039145
27. Jackson RW, Collins SH. Heuristic-based ankle exoskeleton control for co-adaptive assistance of human locomotion. IEEE Trans Neural Syst Rehabil Eng. 2019;27:2059–69.
28. Banala SK, Agrawal SK, Scholz JP. Active leg exoskeleton (alex) for gait rehabilitation of motor-impaired patients. In: 2007 IEEE 10th International Conference on Rehabilitation Robotics. 2007:401–7. 2007 IEEE 10th International Conference on Rehabilitation Robotics.
29. Dinovitzer H, Shushtari M, Arami A. Feedforward control of lower limb exoskeletons: which torque profile should we use? IEEE Robot Autom Lett. 2023;9:382–9.
30. Dinovitzer H, Shushtari M, Arami A. Accurate real-time joint torque estimation for dynamic prediction of human locomotion. IEEE Trans Biomed Eng. 2023;70:2289–97.
31. Shushtari M, Dinovitzer H, Weng J, Arami A. Ultra-robust estimation of gait phase. IEEE Trans Neural Syst Rehabil Eng. 2022;30:2793–801.
32. Shushtari M, Arami A. Human-exoskeleton interaction force estimation in indego exoskeleton. Robotics. 2023;12:66.
33. Carroll K, Kennedy R, Koutoulas V, Bui M, Kraan C. Validation of shoe-worn gait up physilog® 5 wearable inertial sensors in adolescents. Gait & Posture. 2022;91:19–25.
34. Schwameder H, Andress M, Graf E, Strutzenberger G. Validation of an imu-system (gait-up) to identify gait parameters in normal and induced limping walking conditions. In: ISBS-conference Proceedings Archive. 2015.
35. Crouter SE, LaMunion SR, Hibbing PR, Kaplan AS, Bassett DR Jr. Accuracy of the cosmed k5 portable calorimeter. PLoS ONE. 2019;14(12):0226290.
36. Weng J, Hashemi E, Arami A. Human gait cost function varies with walking speed: an inverse optimal control study. IEEE Robot Autom Lett. 2023;8(8):4777–84.
37. Pedotti A, Krishnan VV, Stark L. Optimization of muscle-force sequencing in human locomotion. Math Biosci. 1978;38:57–76.
38. Crowninshield RD, Brand RA. A physiologically based criterion of muscle force prediction in locomotion. J Biomech. 1981;14:793–801.
39. Lieber RL, Roberts TJ, Blemker SS, Lee SSM, Herzog W. Skeletal muscle mechanics, energetics and plasticity. J Neuroeng Rehabil. 2017;14:1–16.
40. Rayssiguie E, Erden MS. A review of exoskeletons considering nurses. Sensors. 2022;22(18):7035.

Shushtari *et al. Journal of NeuroEngineering and Rehabilitation*   (2024) 21:152

Page 20 of 20

41. Blank AA, French JA, Pehlivan AU, O'Malley MK. Current trends in robot-assisted upper-limb stroke rehabilitation: promoting patient engagement in therapy. Curr Phys Med Rehabil Rep. 2014;2:184–95.
42. Guigon E, Chafik O, Jarrassé N, Roby-Brami A. Experimental and theoretical study of velocity fluctuations during slow movements in humans. J Neurophysiol. 2019;121(2):715–27.
43. Brach JS, McGurl D, Wert DM, VanSwearingen J, Perera S, Cham R, Studenski SA. Validation of a measure of smoothness of walking. J Gerontol Se A Biol Sci Med Sci. 2011;66(1):136–41.
44. Bruijn SM, Dieën JH, Meijer OG, Beek PJ. Is slow walking more stable? J Biomech. 2009;42(10):1506–12.
45. Park S-W, Marino H, Charles SK, Sternad D, Hogan N. Moving slowly is hard for humans: limitations of dynamic primitives. J Neurophysiol. 2017;118(1):69–83.
46. Massardi S, Rodriguez-Cianca D, Pinto-Fernández D, Moreno JC, Lancini M, Torricelli D. Characterization and evaluation of human–exoskeleton interaction dynamics: a review. Sensors. 2022;22:3993.
47. Cirstea M, Levin MF. Compensatory strategies for reaching in stroke. Brain. 2000;123(5):940–53.
48. Raghavan P, Santello M, Gordon AM, Krakauer JW. Compensatory motor control after stroke: an alternative joint strategy for object-dependent shaping of hand posture. J Neurophysiol. 2010;103(6):3034–43.
49. Ishmael MK, Gunnell A, Pruyn K, Creveling S, Hunt G, Hood S, Archangeli D, Foreman KB, Lenzi T. Powered hip exoskeleton reduces residual hip effort without affecting kinematics and balance in individuals with above-knee amputations during walking. IEEE Trans Biomed Eng. 2022;70(4):1162–71.

Publisher's Note